Wavelet power spectrum-based autofocusing algorithm for time delayed and integration charge coupled device space camera

Shuping Tao,[1,2,*] Guang Jin,[1] Xuyan Zhang,[1] Hongsong Qu,[1] and Yuan An[1]

[1]Changchun Institute of Optics, Fine Mechanics and Physics, Chinese Academy of Sciences, Changchun, 130033, China

[2]Graduate School of the Chinese Academy of Sciences, Beijing, 100039, China

*Corresponding author: taoshuping11@sina.com

Received 13 April 2012; revised 13 June 2012; accepted 13 June 2012; posted 14 June 2012 (Doc. ID 166269); published 18 July 2012

A novel autofocusing algorithm using the directional wavelet power spectrum is proposed for time delayed and integration charge coupled device (TDI CCD) space cameras, which overcomes the difficulty of focus measure for the real-time change of imaging scenes. Using the multiresolution and band-pass characteristics of wavelet transform to improve the power spectrum based on fast Fourier transform (FFT), the wavelet power spectrum is less sensitive to the variance of scenes. Moreover, the new focus measure can effectively eliminate the impact of image motion mismatching by the directional selection. We test the proposed method's performance on synthetic images as well as a real ground experiment for one TDI CCD prototype camera, and compare it with the focus measure based on the existing FFT spectrum. The simulation results show that the new focus measure can effectively express the defocused states for the real remote sensing images. The error ratio is only 0.112, while the prevalent algorithm based on the FFT spectrum is as high as 0.4. Compared with the FFT-based method, the proposed algorithm performs at a high reliability in the real imaging experiments, where it reduces the instability from 0.600 to 0.161. Two experimental results demonstrate that the proposed algorithm has the characteristics of good monotonicity, high sensitivity, and accuracy. The new algorithm can satisfy the autofocusing requirements for TDI CCD space cameras.

OCIS codes: 100.0100, 280.0280, 070.4790, 100.7410, 100.2960.

1. Introduction

The autofocusing technique is one of the most commonly used techniques for space cameras to ensure high-quality images. With the development of intelligent space cameras, the autofocusing method based on image processing, whose large-scale application will be the inevitable trend, has been adopted for space cameras. As the core of this method is the focus measure and there is no one focus measure that can be applied well in all cases, it is essential to design a robust focus measure with good evaluation capability and stability according to the application. The purpose of this paper is to study a more robust focus measure for time delayed and integration charge coupled device (TDI CCD) space cameras.

To improve the spatial resolution, the TDI mode of CCD is widely used in space cameras. During the TDI mode, the CCD captures an image of a moving object while transferring integrated signal charges synchronously with the object movement. So the effective integration time is increased by a factor of N, which is equal to the number of TDI stages, and the imaging system's sensitivity and signal-to-noise

1559-128X/12/215216-08$15.00/0

ratio (SNR) are improved significantly. Although the TDI mode is used, the spatial resolution cannot be improved if focusing is not done before photographing [1]. Furthermore, the precise focusing is required more for TDI CCD cameras because of the multiple accumulations. However, the scenes imaged by TDI CCD at arbitrary time are different, which makes it difficult to select or develop the focus measure functions. Several focus measures have been studied over the years [1–9]. Obviously, these methods are not applicable for TDI CCD cameras, which either require complex optical systems [1] or are sensitive to noise and other nondefocus factors, such as the scenes and image contrast [2–8]. Many improved focus measures have also been proposed and studied [9–12]. Some of these focus measures, such as centered fourth-order image moments [9] and wavelet-based measures [10], possess good defocus and noise sensitivity. In particular, the wavelet-based measures, which include wavelet band ratio (WBR) and energy of wavelets (EOW), overcome the shortcomings of the moment-based focus measure in the sensitivity to the boundary effect [11]. However, these focus measures are not robust in variable imaging conditions, such as varying illumination [12]. Recently, Tian proposed a focus measure using image phase congruency that is robust for noisy imaging sensors in varying illuminations [12]. Nevertheless, the varying scenes, whose influence is also remarkable in TDI CCD space cameras, are not considered. To eliminate the influence of the varying scenes on the focus measure, a method based on the power spectrum has been studied, and has gotten auspicious results [13–15].

When different scenes are analyzed by the power spectrum in the spatial frequency domain, it can be shown that most arbitrary scenes do indeed theoretically have the same power spectra [16]. This offers a foundation for the power spectrum-based autofocusing methods. However, it is well known that the classical spectrum estimator, fast Fourier transform (FFT) of the autocorrelation function, depends essentially on a good measure of the mean density, disables to preserve the time dependence and describe the evolutionary spectral characteristics of nonstationary processes, and is noise-sensitive [17]. In addition, the image motion mismatching exists in TDI cameras, which also causes a decline in image definition. The FFT spectrum cannot distinguish it from defocus blur flexibly accurately. So developing a robust focus measure that can work for TDI CCD space cameras well is a great challenge.

In this paper, we demonstrate a focus measure using the wavelet power spectrum that is robust for images with varying scenes and image motion mismatching. The new focus measure is introduced in Sections 2 and 4, and it is compared to the FFT spectrum in Section 3. In Section 5, the new focus measure's performance on synthetic images as well as the real ground experiment is shown. The results show that the wavelet spectrum is more suitable for TDI CCD cameras' focus measure.

2. Two-Dimensional Discrete Wavelet Transform Power Spectrum Estimator

Resting on the assumption that the same imaging system's input scene power spectrum is invariant from scene to scene [16], the focus measures for TDI CCD space cameras normally base on the measurements of images' power spectra. This invariance assumption can be obtained from the statistical points distribution theory. When the scene passes through a point detector, a two-dimensional (2D) random density field is produced. Considering a 2D random density field, $I(x,y)$, whose size is $M \times N$, its probability density function (pdf) can be expressed through a Gaussian probability model. In studying a density field's structure, perturbations are used usually, defined as

$$\varepsilon(x,y) = \frac{I(x,y) - I_0}{I_0}, \tag{1}$$

where I_0 is the average. Designate the multiresolution analysis for the 2D square integral function space, $L^2(R)$, to be $\{V_j^2\}_{j\in Z}$. Then only one scaling function exists and corresponds to $\{V_j^2\}_{j\in Z}$, where the scaling function is $\varphi(x,y) = \varphi(x)\varphi(y)$. On the basis of that there is one wavelet function $\phi(x)$ corresponding to one-dimensional (1D) scaling function $\varphi(x)$, the 2D generating wavelet functions $\psi^l(x,y)$ can be decomposed into three parts in the separable case:

$$\begin{aligned} \psi^1(x,y) &= \varphi(x)\phi(y), \\ \psi^2(x,y) &= \phi(x)\varphi(y), \\ \psi^3(x,y) &= \phi(x)\phi(y). \end{aligned} \tag{2}$$

Consequently, the separable and orthonormal discrete wavelet functions, $\psi^l_{i,m;j,n}(x,y)$, can be derived in the 2D space $L^2(R)$.

$$\psi^l_{i,m;j,n}(x,y) = \begin{cases} \varphi_{i,m}(x)\varphi_{j,n}(y), & l = 0 \\ \psi^l_{i,m}(x)\psi^l_{j,n}(y), & l = 1,2,3 \end{cases} \times i,j \geq 0; \quad i,j,m,n \text{ are all integer}, \tag{3}$$

$$\begin{aligned} \psi^l_{i,m}(x) &= \left(\frac{2^i}{M}\right)^{1/2} \psi^l\left(\frac{2^i}{M}x - m\right), \\ \psi^l_{i,n}(y) &= \left(\frac{2^i}{N}\right)^{1/2} \psi^l\left(\frac{2^i}{N}y - n\right). \end{aligned} \tag{4}$$

Equations (3) and (4) show that the wavelet functions are families of functions that are generated by dilating the generating wavelet by a factor of $(2^i, 2^j)$, and by translating $\psi^l(x,y)$ by (m,n). Furthermore, the wavelet functions are orthogonal to both dilation and translation.

Therefore, a 2D signal with finite size can be broken down into a series of subchannels' 2D signals after the periodic extension:

$$\varepsilon(x,y) = \sum_{i,j=0}^{\infty} \sum_{m,n=-\infty}^{\infty} \sum_{l=0}^{3} w_{i,j}^{l}(m,n)\psi_{i,m;j,n}^{l}(x,y). \quad (5)$$

Here, $w_{i,j}^{l}(m,n)$, namely the 2D discrete wavelet coefficients, are the decomposition coefficients of $\varepsilon(x,y)$, corresponding to the orthogonal basis $\psi_{i,m;j,n}^{l}(x,y)$. So combining with Eq. (3), the wavelet coefficients can be derived as follows:

$$w_{i,j}^{l}(m,n) = \sum_{x=-\infty}^{\infty} \sum_{y=-\infty}^{\infty} \varepsilon(x,y)\psi_{i,m;j,n}^{l}(x,y), \quad (6)$$

where w^0 denotes the low-frequency components, w^1 denotes the high-frequency components in horizontal orientation, w^2 denotes the high-frequency components in vertical orientation, and w^3 denotes the high-frequency components in diagonal orientation. The Parseval's theorem relates the power for a distribution to the discrete wavelet coefficients [18]; this yields

$$\frac{1}{MN}\sum_{x=1}^{M}\sum_{y=1}^{N}|\varepsilon(x,y)|^2 = \sum_{i,j=0}^{\infty}\frac{1}{MN}\sum_{m=0}^{2^i-1}\sum_{n=0}^{2^j-1}\sum_{l=0}^{3}|w_{i,j}^{l}(m,n)|^2. \quad (7)$$

Then we get the computation formula for the wavelet power spectrum in scale (i,j) as follows:

$$P_{i,j} \equiv \frac{1}{MN}\sum_{m=0}^{2^i-1}\sum_{n=0}^{2^j-1}\sum_{l=0}^{3}|w_{i,j}^{l}(m,n)|^2. \quad (8)$$

Taking the calibration images derived by one TDI CCD prototype camera in the laboratory for example, three selected images are decomposed by a 2D wavelet in level of three for comparison, as shown in Fig. 1. Here, the high-frequency coefficients are enlarged to highlight.

In Figure 1, the three images' imaging parameters are the same, except for the focusing codes. In panel (a), the edges of wavelet component images are clear, and the transition is quick; in panel (b), the transition tends to fade; and in panel (c), the edges have blurred. This characteristic just corresponds to the image quality; therefore the wavelet components can be used for image quality analysis.

Image motion mismatching and defocusing are the two major factors that cause the blurred images for the push-broom TDI CCD cameras. The confusion in two blurs may result in wrong estimation for the focus measure. Fortunately, their principles of causing blurs are different [19–21]. The speed deviation along the track, one of the image motion mismatching velocity vectors, is most likely to occur. The speed deviation results in not only the images' stretching or squashing, but also the charge added together no longer corresponding to the same imaging target. So the image motion mismatching drops the modulation transfer function (MTF) by

$$\mathrm{MTF}_{\mathrm{match}} = \frac{\sin\left(\frac{\pi}{2}N\frac{v_c}{v_N}\frac{\Delta v_P}{v_P}\right)}{\frac{\pi}{2}N\frac{v_c}{v_N}\frac{\Delta v_P}{v_P}}, \quad (9)$$

where N is the number of TDI stages, v_c is the characteristic frequency, which usually equals the Nyquist frequency v_N, and $\Delta v_P/v_P$ is the velocity resident error of the image motion matching. As $\Delta v_P/v_P$ is a vector with the direction along the track, we can easily get that $\mathrm{MTF}_{\mathrm{match}}$ is the MTF in the along-track direction. Thus, the image motion mismatching affects the images' sharpness in the along-track direction as one low-pass filter, but the sharpness in the across-track direction is not be affected, as shown in Fig. 2 (the image motion mismatching image and its 2D DWT). The difference can be found in Fig. 2, especially by the edges, where the vertical edges are sharp while the horizontal edges get blunt.

The principle of defocusing is that all target points through the optical system become diffusion spots in the focal plane, affected by the point spread function (PSF). The MTF of optical defocusing is analyzed in Subsection 4.A. According to Eq. (17), the MTF of defocusing is a function of two orthogonal variables u and v. Thus, the MTF of defocusing is omnidirectional in the 2D space, and defocusing performs

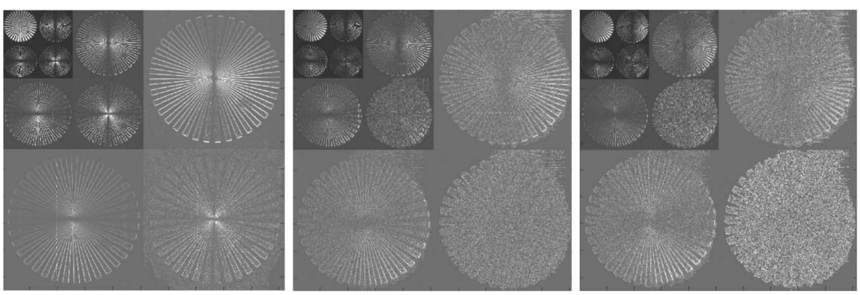

Fig. 1. 2D DWT for three images with different defocusing amount: (a) relative focusing code is 0; (b) relative focusing code is 30; and (c) relative focusing code is 60.

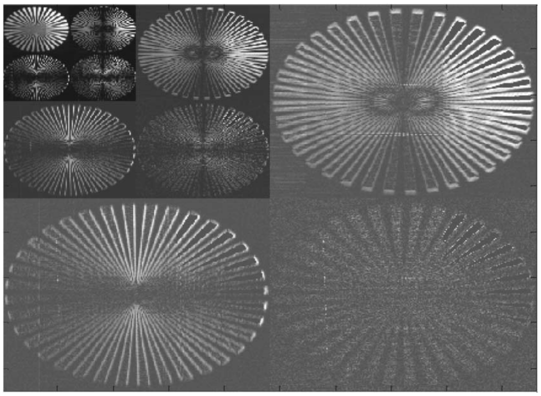

Fig. 2. Image motion mismatching image and its 2D DWT.

on images to be fuzzy in any direction, as shown in Fig. 1(c), where the edges in all directions get blurred. Through above analysis, we can draw a conclusion that the changes of high-frequency components across the track depend mainly on defocusing; however, the changes of high-frequency components along the track are influenced by both defocusing and image motion mismatching. So if the high-frequency components only across the track are obtained and applied, the impact of image motion mismatching on the evaluation for defocusing can be eliminated effectively. Hence, the evaluation accuracy can be improved as well. Thus, the power spectrum estimation formula in scale (i, j) becomes

$$P_{i,j} \equiv \frac{1}{MN} \sum_{m=0}^{2^i-1} \sum_{n=0}^{2^j-1} |w_{i,j}^1(m,n)|^2. \tag{10}$$

3. Comparison of the DWT Spectrum to the FFT Spectrum

Traditionally, the power spectrum is calculated by the Fourier transform of the autocorrelation function. The Fourier expression coefficients for a density field can be derived easily, as shown in Eq. (11), and then the relation of the signal's power and Fourier coefficients can also be derived easily according to the Parseval's theorem, as Eq. (12):

$$F(u,v) = \frac{1}{MN} \sum_{x=1}^{M} \sum_{y=1}^{N} \varepsilon(x,y) e^{-2\pi i y \frac{v}{N}} e^{-2\pi i x \frac{u}{M}}, \tag{11}$$

$$\frac{1}{MN} \sum_{x=1}^{M} \sum_{y=1}^{N} |\varepsilon(x,y)|^2 = \sum_{u=-\infty}^{\infty} \sum_{v=-\infty}^{\infty} |F(u,v)|^2. \tag{12}$$

So the Fourier power spectrum density defines as

$$P(u,v) = |F(u,v)|^2. \tag{13}$$

For the convenience of comparing the power spectra of different images, the 2D power spectrum is converted to its logarithm and in one-dimension, as follows:

$$P(\rho) = \log\left(\frac{1}{n_\rho \mu^2 MN} \sum_{\theta=-\pi}^{\pi} |F(\rho,\theta)|^2\right), \tag{14}$$

where $F(\rho,\theta)$ are the polar coordinates for $F(u,v)$, ρ is frequency referred to the radial distance, $\rho = \sqrt{u^2+v^2}/\sqrt{(M/2)^2+(N/2)^2}$, in units of cycles/pixel, n_ρ is the total number of the points with radial distance ρ, and μ^2 denotes the DC power to eliminate the influence of images' brightness changing. The conversion schematic diagram is shown in Fig. 3. We take the image size $M = N$ in the experiments. As shown in Fig. 3, the 2D power spectra on the circle are incomplete when the cycle's radial distance ρ is greater than 0.707, where $\rho = 0.707$ cycles/pixel corresponds to the largest inscribed circle. Thus the truncation brings a sharp transition at 0.707 cycles/pixel in the one-dimensional (1D) power spectrum.

Figure 4 is one real remote sensing image; because the focus measure rests on the comparison of the adjacent images, we select its four adjacent subpictures along the push-bloom direction for the analysis. Then we get the power spectrum results, as shown in Figs. 5(a) and 5(b), using the traditional FFT and the proposed DWT spectrum estimator, respectively.

Figure 5 shows that the different scenes' power spectra estimated by two methods both keep invariant well. However, compared with the FFT spectrum estimator, the DWT power spectrum estimator performs better in scene independence. Obviously, a large river area is contained in subpicture 3. Consequently, the FFT spectrum curve of subpicture 3 is much lower than the other FFT spectrum curves of the subpictures that contain abundant information. Nevertheless, the DWT spectrum curves of all subpictures keep a good invariance property. Moreover, the invariance of the DWT spectrum performs better in the high frequency. Besides, by overcoming the shortage of FFT in a single resolution, the DWT is more suitable for the TDI CCD camera's focus measure.

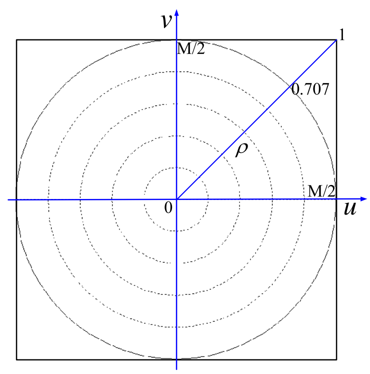

Fig. 3. (Color online) Schematic diagram of 2D power spectrum to 1D conversion. The 1D power spectrum is generated by averaging the power contained within cycles of radial distance. The radial distance $\rho = 0.707$ cycles/pixel corresponds to the largest inscribed circle of the 2D power spectrum.

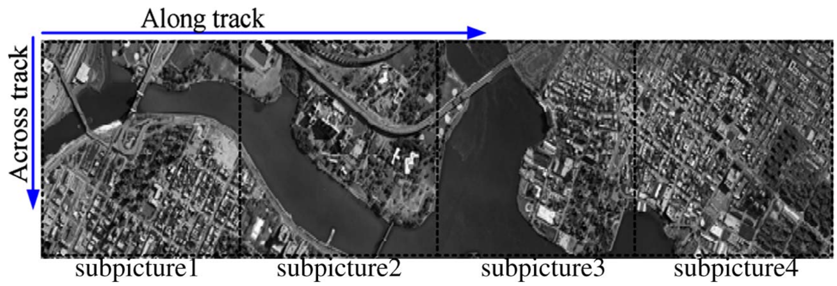

Fig. 4. (Color online) Image taken by some TDI CCD aeronautic camera.

4. Focus Measure based on DWT Spectrum Estimator

A. Change of Power Spectrum Caused by Defocusing

The model of the imaging system is given as follows:

$$I(x,y) = f(x,y) \otimes h(x,y), \tag{15}$$

where $f(x,y)$ is the input image and $h(x,y)$ is the PSF. The MTF corresponding to defocusing is the FFT of PSF. Here we assume all the other sections' MTF to be 1, and consider the brightness in the confusion circle is uniform from the geometrical optics. The PSF is approximated by the 2D Gaussian function is

$$h(x,y) = \begin{cases} 1/\pi R^2, & x^2+y^2 \le R^2 \\ 0, & x^2+y^2 > R^2 \end{cases}. \tag{16}$$

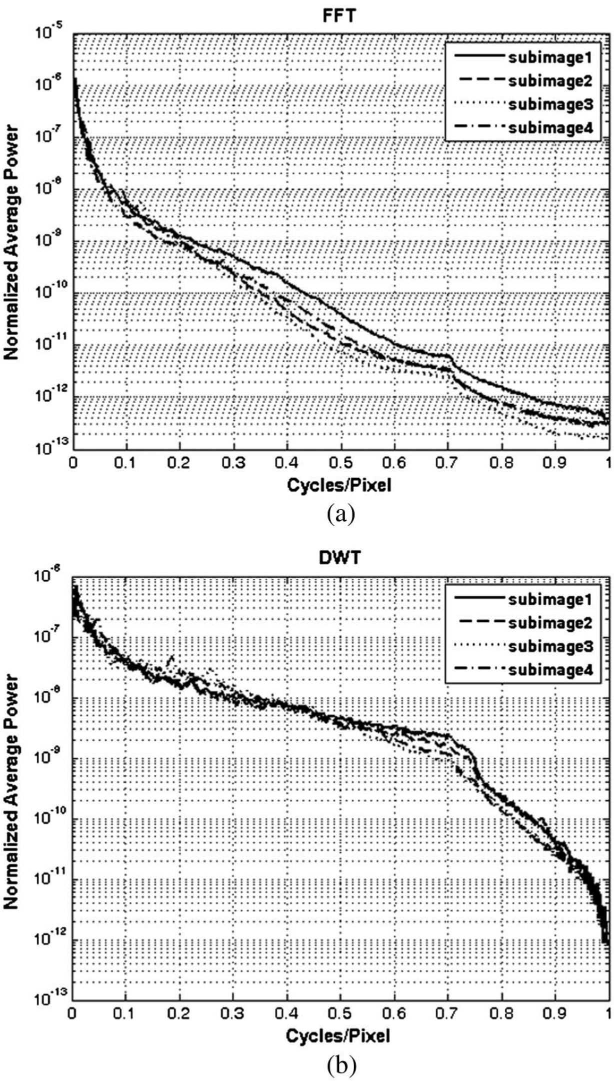

Fig. 5. Normalized power spectra for the four subpictures in Fig. 3: (a) FFT spectrum; (b) the proposed DWT spectrum.

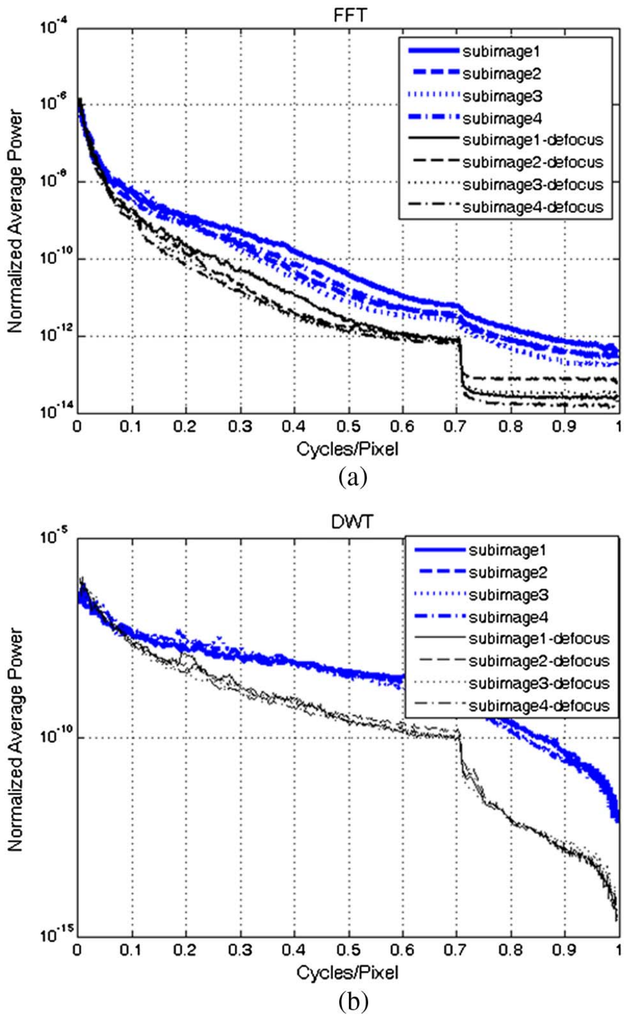

Fig. 6. (Color online) Power spectra of focusing and defocusing images. (a) FFT power spectra; (b) DWT spectra. The bold lines in upside correspond to the four focusing subpictures, and the thin lines in downside correspond to their defocusing images. The sharp transitions at 0.707 cycles/pixel are caused by the 2D power spectra to 1D conversion.

So the optical transfer function gets

$$H(u,v) = \exp\left[-\frac{1}{2}\rho^2(u,v)a^2\right]. \tag{17}$$

According to the above analysis, the PSF is almost the same as one low-pass filter, and the cut-off frequency changes with the defocusing amount. Thus, the cut-off frequency gets higher as the focusing gets more accurate.

According to the Eq. (15), the 1D power spectrum of the output image gets to be

$$\begin{aligned} P(\rho) &= \frac{1}{n_\rho \mu^2 MN} \sum_{\theta=-\pi}^{\pi} |T(F(f(x,y) \otimes h(x,y)))|^2 \\ &= \frac{1}{n_\rho \mu^2 MN} \sum_{\theta=-\pi}^{\pi} |T(F(f(x,y)) \times F(h(x,y)))|^2 \\ &= \frac{1}{n_\rho \mu^2 MN} \sum_{\theta=-\pi}^{\pi} T(|F(u,v)|^2) \times T(|H(u,v)|^2). \end{aligned} \tag{18}$$

So for the same input image, if the defocusing gets more serious, the output image will become fuzzier in the space domain, and the high frequency will lose more in the frequency domain. In order to validate the change of the power spectrum caused by defocusing, we derive the defocusing image from the image in Fig. 4, and then their power spectra are analyzed, as shown in Fig. 6. It shows that the changes of two kinds of power spectra are similar; that is, defocusing makes the high frequency lost. So we can take the sum of the high frequency in power spectra to build the focus measure function. And here we find the foundation of the focus measure for TDI CCD space cameras.

B. Focus Measure Function

As shown in Fig. 6, defocusing makes the high frequency lost, while it almost has no effect on the low frequency. So we select the sum of power spectra (PSS) between 0.05 and 0.5 cycles/pixel for the focus measure function, as shown in Eq. (19):

$$Q_{\mathrm{PSS}}^{(1)} = \sum_{\rho=0.05}^{0.5} P_{i,j}. \tag{19}$$

After analyzing the defocusing model, we can draw a conclusion that if the weight of high frequency increases and the weight of low frequency decreases, the focus measure function will be more accurate and sensitive. So the frequency is chosen as the weighting factor in this paper, and the focus measure function is improved as follows:

$$Q_{\mathrm{PSS}}^{(2)} = \sum_{\rho=0.05}^{0.5} \rho P_{i,j}. \tag{20}$$

5. Experiment Results and Analysis

To validate the proposed algorithm, we choose images with different scenes as samples, such as the 25 different subpictures shown in Fig. 7. To simulate the real imaging of TDI CCD space cameras adequately, the defocusing amounts are set to be different for each subpicture. Here we suppose that the AF encoder position corresponding to the original image is zero. The step is set as 0.5, 1, 1.5, 2, and 3, respectively; then a series of images with different defocusing amounts and diverse scenes is obtained. The evaluation results for these images by two focus measures are shown in Fig. 8 and Table 1.

In Table 1, the error number is the number of the points that don't satisfy with monotonicity. Here we get the slopes of the total 25 data by the difference operator 1. So the data points located in the left side of the center with slopes no greater than 0 and those located in the right side of the center with slopes no less than 0 can be considered as error. However, there are some consecutive error points that even meet the above monotonicity. So in order to reduce the missing rate for the error points, the result is corrected using the difference operator 2, and we get the final count to be error number. Error ratio is the result of error number divided by total number.

The results show that the focus measure based on the DWT spectrum meets the principle of monotonicity well, and it precedes the FFT spectrum-based method. Compared to the FFT spectrum-based focus measure, the difference of the values calculated by the DWT spectrum-based focus measure gets larger in the same state, so the DWT spectrum-based focus measure meets the principle of high sensitivity. The average error ratio decreases from the FFT spectrum-based focus measure's 0.4 to 0.112, so the DWT spectrum-based focus measure meets the principle of high accuracy. In addition, comparing the

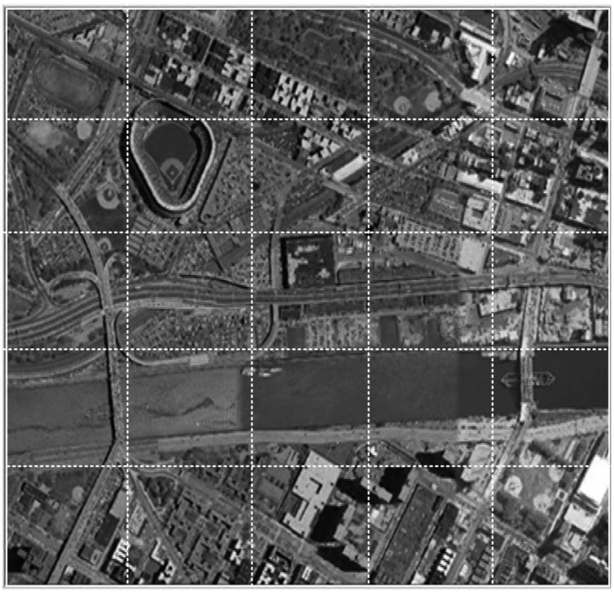

Fig. 7. Experiment samples.

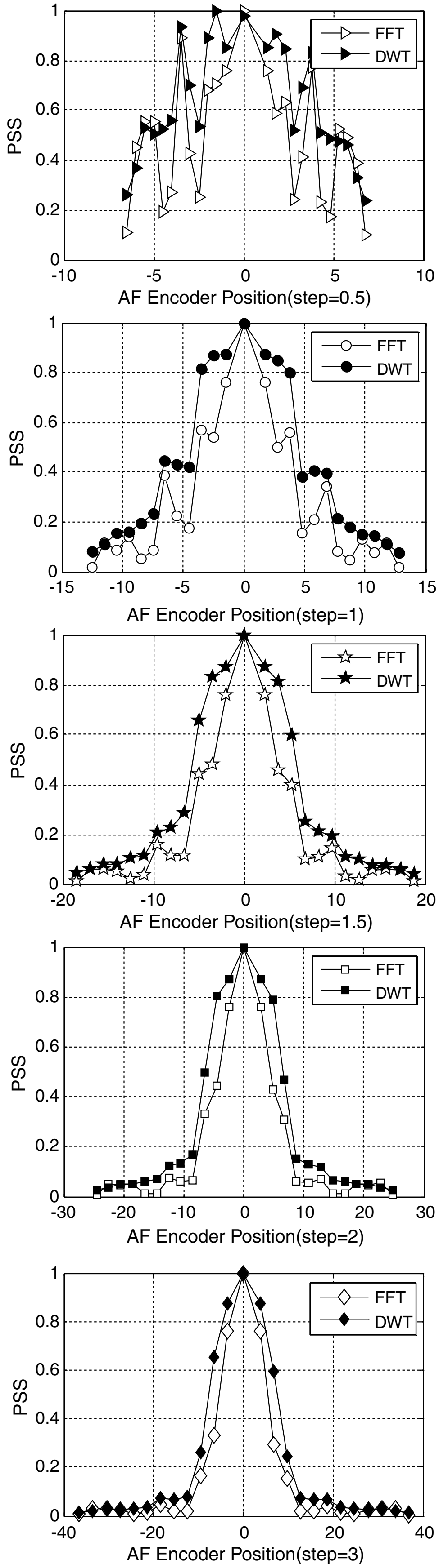

Fig. 8. Comparison of two methods' definition evaluation results for images with different scenes and defocusing amounts.

Table 1. Error Ratio for Two Methods

	The DWT-Based Method		The FFT-Based Method	
Step	Error Number	Error Ratio	Error Number	Error Ratio
0.5	7	0.28	12	0.48
1	3	0.12	12	0.48
1.5	0	0	9	0.36
2	1	0.04	8	0.32
3	3	0.12	9	0.36

Table 2. STD of Two Focus Measures

Relative Focusing Code	STD_DWT	STD_FFT
2	0.16100	0.60485
25	0.16100	0.60485
50	0.16100	0.60485
75	0.16181	0.60323
100	0.16160	0.59948
150	0.16137	0.59573

curves shown in Fig. 8, we can know that the DWT spectrum-based measure curves are more saturated. Thus, the proposed focus measure based on the DWT spectrum is more efficient and better for TDI CCD space cameras.

Then tests are implemented on ground experiments, for one TDI CCD prototype camera. To compare two focus measures' performances, 80 random images are gathered in every setting relative focusing code respectively, and the standard deviation (STD) of 80 images' power spectra are calculated, as shown in Table 2.

In Table 2, STD_DWT presents the STD of the evaluation results using the DWT spectrum-based method. Likewise, STD_FFT presents the STD of the evaluation results using the FFT spectrum-based method. The results show that an STD of 0.161 can be obtained with the DWT power spectrum-based method, while that of the FFT spectrum-based measure is as high as 0.600. Obviously, the proposed focus measure performs better in the stability, since it is less sensitive to the scene changing. In conclusion, the new algorithm is more suitable for TDI CCD space cameras than the old FFT solution.

6. Conclusion

The autofocusing algorithm in this work is proposed for the real-time autofocusing needs of TDI CCD space cameras. Compared to other conventional focus measures, the FFT power spectrum-based method has achieved preliminary results, which is relatively more robust for the images with real-time changing scenes caused by TDI CCD cameras. However, the FFT spectrum-based focus measure cannot separate the defocusing blur from the image motion mismatching blur, and it has the noise-sensitive and other defects. The proposed algorithm improves the FFT spectrum-based method. Firstly, the formula of wavelet power spectrum is derived from the 2D DWT and the Parseval's theorem. Then the blurred images caused by image motion mismatching are analyzed with DWT, and the directional power spectrum estimator is obtained afterwards, which can effectively separate the effect of image motion mismatching on the defocusing judgment. Finally, in order to further improve the algorithm, the weighted sum of power spectrum between 0.05 and 0.5 cycles/pixel is selected for focus measure. The experimental results indicate that the average error ratio can drop to 0.112, while that of the prevalent algorithm based on FFT spectrum is 0.4. Besides, the new algorithm can decrease the instability from 0.60 to 0.161. The focus measure in this work has been proved to have the characteristics of good monotonicity, high sensitivity, and accuracy, and can meet the autofocusing requirements of TDI CCD space cameras.

I deeply thank my supervisor, Prof. G. Jin, whose help, advice, and supervision are invaluable. I also thank all the colleagues in my laboratory, with whom the ground experiments were carried out successfully. Finally, I would like to thank X. Y. Zhao, a Ph.D. student at the University of Toronto. His help in the English writing is greatly acknowledged.

References

1. Z. H. Li and K. Y. Wu, "Autofocus system for space cameras," Opt. Eng. **44**, 053001 (2005).
2. J. F. Brenner, B. S. Dew, J. B. Horton, T. King, P. W. Neurath, and W. D. Selles, "An automated microscope for cytologic research a preliminary evaluation," J. Histochem. Cytochem. **24**, 100–111 (1976).
3. D. Vollath, "Automatic focusing by correlative methods," J. Microsc. **147**, 279–288 (1987).
4. M. Subbarao, T. Choi, and A. Nikzad, "A Focusing techniques," Opt. Eng. **32**, 2824–2836 (1993).
5. H. C. Zhang, C. Gould, B. Roberts, and M. McQuillan, "An objective image focus monitor for CD-SEM," Proc. SPIE **6922**, 692226 (2008).
6. C. M. Chen, C. M. Hong, and H. C. Chuang, "Efficient autofocus algorithm utilizing discrete difference equation prediction model for digital still cameras," IEEE Trans. Consumer Electron. **52**, 1135–1143 (2006).
7. T. Aydin and Y. S. Akgul, "An occlusion insensitive adaptive focus measurement method," Opt. Express **18**, 14212–14224 (2010).
8. M. Kristan, J. Pers, M. Perse, and S. Kovaci, "A Bayes-spectral-entropy-based measure of camera focus using a discrete cosine transform," Pattern Recog. Lett. **27**, 1431–1439 (2006).
9. Y. N. Zhang, Y. Zhang, and C. Y. Wen, "A new focus measure method using moments," Image Vision Comput. **18**, 959–965 (2000).
10. Y. B. Tian, S. Kevin, and C. F. Wildsoet, "Performance of focus measures in the presence of nondefocus aberrations," J. Opt. Soc. Am. A **24**, B165–B173 (2007).
11. J. Kautsky, J. Flusser, B. Zitová, and Ŝ. Simberová, "A new wavelet-based measure of image focus," Pattern Recog. Lett. **23**, 1785–1794 (2002).
12. Y. B. Tian, "Autofocus using image phase congruency," Opt. Express **19**, 261–270 (2011).
13. NASA Glenn Research Center, "A compact microscope imaging system with intelligent controls," https://technology.grc.nasa.gov/tech-detail-coded.php?cid=GR-0047.
14. Z. B. Zhao and J. H. Liu, "Power spectra based auto-focusing method for airborne optoelectronic platform," Acta Optica Sinica **30**, 3495–3500 (2010).
15. M. E. Rudnaya, R. M. M. Mattheij, J. M. L. Maubach, and H. G. ter Morsche, "Orientation identification of the power spectrum," Opt. Eng. **50**, 103201 (2011).
16. N. B. Nill and B. H. Bouzas, "Objective image quality measure derived from digital image power spectra," Opt. Eng. **31**, 813–825 (1992).
17. Z. G. Fan, S. Q. Chen, H. L. Hu, H. Chang, and Q. Fu, "Autofocus algorithm based on wavelet packet transform for infrared microscopy," in *Proceedings of IEEE Conference on Image and Signal Processing* (IEEE, 2010), pp. 2510–2514.
18. J. Pando and L. Z. Fang, "Discrete wavelet transform power spectrum estimator," Phys. Rev. E **57**, 3593–3601 (1998).
19. Y. Yitzhaky, I. Mor, A. Lantzman, and N. S. Kopeika, "Direct method for restoration of motion-blurred images," J. Opt. Soc. Am. A **15**, 1512–1519 (1998).
20. R. V. Shack, "The influence of image motion and shutter operation on the photographic transfer function," Appl. Opt. **3**, 1171–1181 (1964).
21. J. Q. Wang, P. Yu, C. X. Yan, J. Y. Ren, and B. He, "Space optical remote sensor image motion velocity vector computational modeling, error budget and synthesis," Chin. Opt. Lett. **3**, 414–417 (2005).